International Journal for Numerical Methods in Biomedical Engineering

WILEY

BASIC RESEARCH OPEN ACCESS

Can a Cochlear Implant Be Used as an Electrical Impedance Tomography Device?

Friedemarie Fourie | Joshua Thiselton | Tania Hanekom

Bioengineering, Department of Electrical, Electronic and Computer Engineering, University of Pretoria, Gauteng, South Africa

Correspondence: Tania Hanekom (tania.hanekom@up.ac.za)

Received: 28 March 2024 | **Revised:** 18 November 2024 | **Accepted:** 29 December 2024

Funding: This work is based on the research supported in part by the National Research Foundation of South Africa (Grant number 141954).

Keywords: cochlear implant | electrical impedance tomography (EIT) | image reconstruction | inverse problem parameterisation | modelling | regularisation

ABSTRACT

The imaging of the live cochlea is a challenging task. Regardless of the quality of images obtained from modern clinical imaging techniques, the internal structures of the cochlea mainly remain obscured. Electrical impedance tomography (EIT) is a safe, low-cost alternative medical imaging technique with applications in various clinical scenarios. In this article, EIT is investigated as an alternative method to image and extract the centre of gravity of the modiolus in vivo. This information can be used to augment present postoperative medical imaging techniques to investigate the cochlea. The cochlear implant EIT system was simulated by modelling user-specific electrode array trajectories within a simple conductive medium containing an inhomogeneity representing the modiolus. The method included an adapted adjacent stimulation protocol for data collection. For the image reconstruction, NOSER and Tikhonov priors were considered. A parameter analysis was conducted to find the most robust combination of image priors and hyperparameters for this application. The cochlear implant EIT methodology was validated at different noise levels for four electrode array trajectories. Comparing the NOSER and Tikhonov priors, it was observed that the NOSER prior exhibits superior centre of gravity localisation performance in cochlear implant EIT image reconstruction for different noise levels and user-dependent variability in electrode array trajectories. Image reconstruction, using a NOSER prior at a hyperparameter value of approximately 0.001, resulted in an average centre of gravity localisation error of less than 4% for all electrode array trajectories using difference imaging and less than 5.5% using absolute imaging.

1 | Introduction

The postoperative imaging of the cochlea after the insertion of a cochlear implant (CI) is advised to gain insight into the electrode placement within the cochlea and investigate potential complications [1]. These images also form the basis for three-dimensional (3D) computational modelling of the user-specific biophysics of the electrically stimulated cochlea and the consequent excitation behaviour of the auditory neurons. The predictive outcomes from these models are greatly influenced by unique cochlear morphology. The level to which morphology can be incorporated into the models depends on the quality of the available cochlear scans from which the models are derived [2]. The in vivo investigation of user-specific cochlear morphology is challenging, as the available postoperative imaging techniques present limitations in terms of resolution and distinguishability. Typical postoperative imaging includes computed tomography (CT) techniques such as high-resolution CT (HRCT) and cone-beam CT (CBCT). CBCT scans provide good spatial resolution, but variations in image quality among different scanners may affect the distinguishability of cochlear structures [1]. Regardless of the quality of the image, the internal structures of the cochlea are typically obscured. The modiolar region, including the modiolar wall of the cochlear canal, is rarely visible. As this is the region in which the nerve fibres exist,

an alternative to existing imaging techniques that may augment information on the user-specific internal structures of the cochlea will be beneficial in the context of computational modelling.

Electrical impedance tomography (EIT) is a safe, low-cost alternative to various medical imaging techniques, posing no known hazards to the user [3]. It functions by measuring the electrical impedance between electrodes placed around a cross-section of the imaged structure to generate a 2D contour map of the internal impedance distribution. The stimulation protocol is similar to that of a CT in that a perimetral array of probing and measurement elements are systematically activated [4]. As tissue types have different impedances [5], the impedance distribution map can be used to estimate the areas occupied by each tissue type. EIT also has the capability for 3D approximations. This involves injecting sinusoidal impulses across a 2D cross-section and using a more complex reconstruction algorithm to estimate impedances further away from the measurement plane. The accuracy of the generated image decreases with increased distance from this plane [6].

Unlike more established imaging methods, there is no standardised image reconstruction method for EIT. Various stimulation protocols and reconstruction algorithms are available, each with situational drawbacks. This article explores potential solving strategies, meshing techniques and image-processing methods to propose a robust implementation basis for using a CI as an EIT device to image the cochlear modiolus.

On a high level, CI and EIT hardware consists of similar components, as illustrated in Figure 1. The internal unit of the CI consists of a receiver-stimulator (containing a current source and back telemetry unit) and an electrode array [7]. Traditionally, an EIT data acquisition unit consists of a current source, similar to the internal unit of the CI, and a boundary voltage measurement unit. Importantly, most commercial CI units allow for the implementation of unique stimulation and measurement patterns, as required for precise tuning of the device [8]. This means that an EIT measurement protocol can be implemented on implanted devices with an accessible back telemetry system.

Traditionally, EIT electrodes are placed around an irregular boundary of a large anatomical structure such as the thorax. However, there are existing EIT applications that have a similar scale and environment to that of a CI. Electrical impedance endotomography involves an internal probe placed in the centre of the region of interest (ROI) and has been applied in transrectal EIT for prostate screening [9]. Internal electrode arrays are also commonly employed in neural EIT for functional imaging of the brain [10–14]. In a previous study, the feasibility of internal micro-electrode arrays implanted in a rat thalamus was investigated in simulation. The method could reliably reconstruct and localise visually evoked impedance changes in the visual subcortical bodies within 300 μm from the electrode array [10].

The key differences in the CI application compared to previous EIT studies relate to the positioning of the electrodes, the

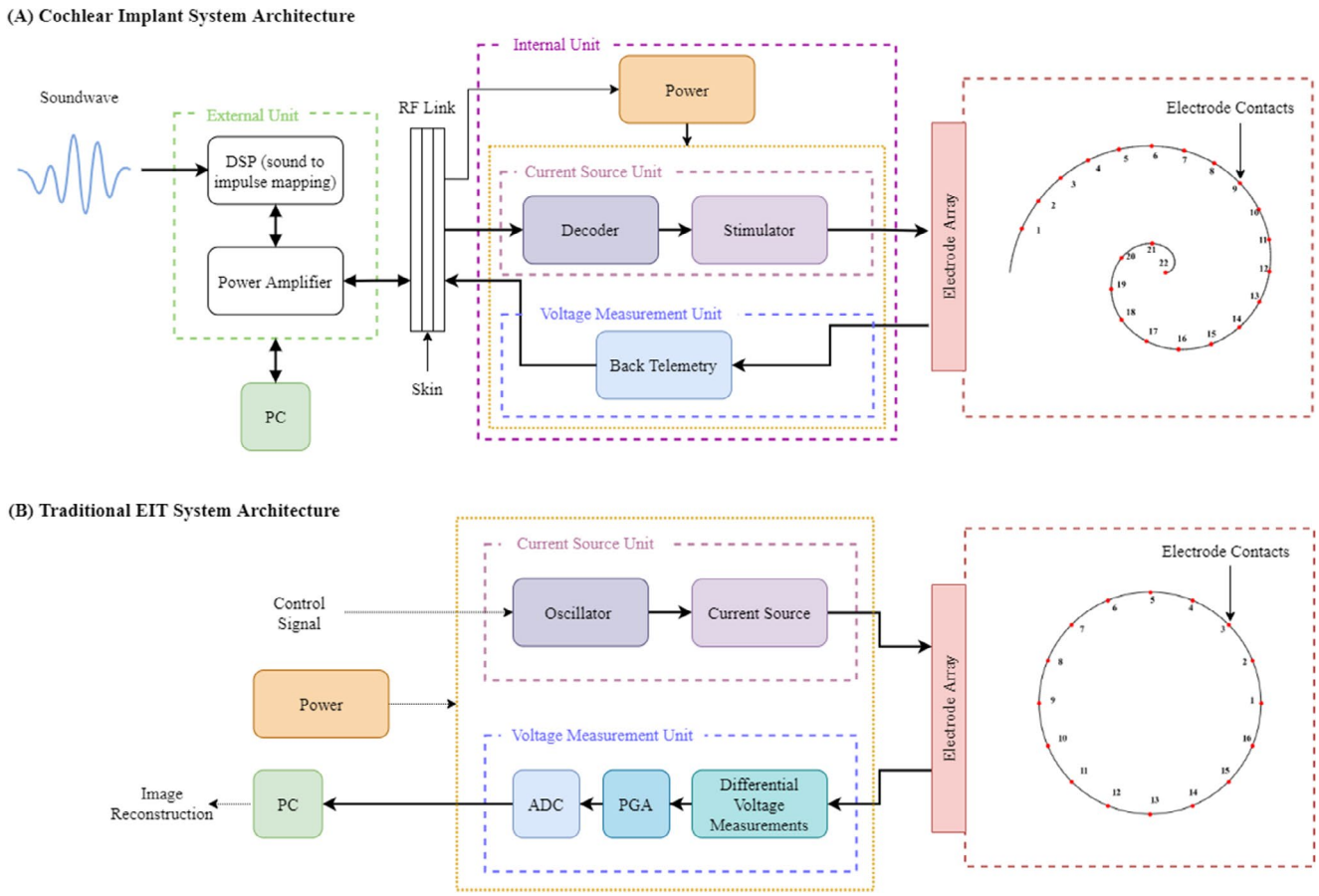

FIGURE 1 | The system architecture of (A) CI devices [7] and (B) traditional EIT systems.

conductivity of the medium in contact with the electrodes and the stimulus waveform. In traditional EIT systems, care is taken to align the electrodes in a specific plane, which is not possible with CI electrode arrays due to the 3D spiralling nature of the cochlea. The electrodes are also not necessarily equally spaced, nor does the final electrode lie adjacent to the first. The CI electrode also seldom touches the medial wall of the cochlear canal and is instead separated from the modiolus by a conductive layer of perilymph. This may distort the measured impedance matrix and reduce the accuracy of the imaging [15]. Lastly, traditional EIT uses sinusoidal stimulus waveforms, while CI systems are typically only able to deliver bipolar pulsatile waveforms.

To assess whether CI-EIT imaging is viable despite the differences relative to traditional EIT mentioned above, the accuracy of measuring the location of the modiolar axis is explored. The modiolar axis is a key parameter in reliably and unambiguously describing and referencing morphological parameters for clinical and modelling applications. The modiolar axis is commonly defined as the line between the helicotrema and the centre of gravity (CoG) of the modiolus in the basal turn. However, inter-observer variability can lead to misalignment and the subsequent inaccurate quantification of other landmarks [16]. The modiolar CoG is, accordingly, an important geometric property to be determined reliably and robustly. As the CI electrode array mostly occupies the basal turn of the cochlea, EIT may provide a reliable method to determine the CoG of the basal turn by eliminating inter-observer errors. It could also be used for co-registration of different cochlear imaging modalities and serve as a reference to observe structural changes of cochlear anatomy post-implantation [17].

This article presents a simulation study that assesses the viability of and serves as a foundation for the future implementation of a CI-EIT system in clinical applications. To this end, a robust stimulation protocol and image reconstruction technique was developed that uses an implantee's own uniquely placed CI electrode array as the EIT electrode system. The accuracy with which the CoG of the modiolus could be determined served as a measure to determine a suitable EIT strategy for implementation with a CI system.

2 | Materials and Methods

The CI-EIT system is based on the same principles as traditional EIT by implementing a current source driven stimulation pattern and measuring the associated voltage distribution within the cochlea to generate a reconstructed conductivity image [3]. A model representing the electrode placement, geometry of the structure of interest and the stimulation and measurement protocol is an integral part of the EIT image reconstruction process. For the simulation study, the measurement environment is replaced by a model to simulate data retrieved from the electrodes. Accordingly, two models involving the specific geometry and electrode locations are required. The first model is used for the forward solution to generate simulated data, while the second model is used for the image reconstruction process. The CI-EIT system implements a stimulation and measurement protocol adapted from standard techniques to generate simulated measurements and integrate them into the reconstruction process. EIDORS v3.10, a versatile open-source software suite for EIT image reconstruction [18], was used in this study. The methodology is analysed and validated in terms of the CoG localisation errors.

2.1 | CI Electrode Model Construction

The key consideration of this study is to investigate the viability of translating the proposed CI-EIT system to clinical application for assessing the characteristics of the modiolus and its surrounding structures. Cochlear Ltd. provides a platform for custom back telemetry implementations, which enables the CI device to be employed as the data acquisition unit of the proposed CI-EIT system. To this end, it was decided to implement CI electrode array models conforming to the key features of the Cochlear Nucleus CI24RE. These models incorporate the 22 half-banded electrode contacts of the Cochlear Nucleus CI24RE, typically manufactured using a biocompatible platinum-iridium alloy [7], but do not consider the tapering of the electrode array towards the apical end.

In traditional EIT systems, great care is taken to align the electrodes in a specific plane, which is not possible with CI electrode arrays due to the 3D spiralling nature of the cochlea. The shape and degree to which the vertical displacement of the electrodes occurs vary among different CI users, as each cochlea exhibits unique shape and coiling characteristics [19]. The CI electrode array trajectories of four different CI users were sampled to gain a better understanding of the variables influencing CI-EIT reconstruction and localisation performance.

Person-specific electrode array trajectory coordinates were obtained from landmark data extracted from user CT scans. These trajectories were used to construct models in the finite element analysis software COMSOL Multiphysics v5.5. The four electrode array models will be referred to as Electrode 1, 2, 3 and 4, respectively, shown in Figure 2. From Figure 2A, the difference in shape among the four electrodes can be observed, while Figure 2B illustrates the variability in the vertical distribution of the electrodes within the arrays.

All the electrodes were embedded in a cylindrical volume with an 8 mm height and radius. An inhomogeneity was added to the model to simulate the modiolus and auditory nerve. The modiolus was simulated by a cylinder with a radius of 1 mm and height of 8 mm, with the auditory nerve as a cylinder embedded in the former, with a radius of 0.5 mm and height of 8 mm. The complete model setup is shown in Figure 3. The size of the simulated modiolus relative to the electrode array was purposefully understated. This will allow for the placement of the inhomogeneity at various locations within the electrode array to verify the localisation accuracy and sensitivity of the CI-EIT system.

The various conductivity and electrode contact impedance values were set to represent values typically observed in the cochlear environment. The conductivities were set to values obtained from literature, as summarized in Table 1. The cochlear fluid was assigned the average conductivity value of the endolymph and perilymph as obtained from the literature [20].

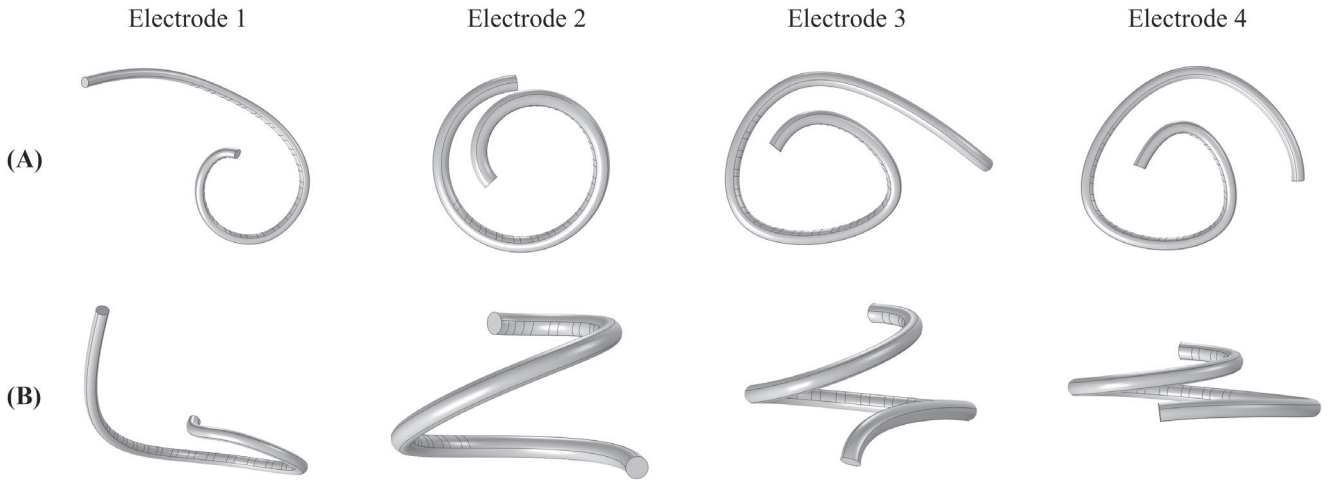

FIGURE 2 | The four person-specific electrode array models with unique trajectories as generated in COMSOL, from left to right: Electrode 1, Electrode 2, Electrode 3 and Electrode 4. (A) Top view of Electrode 1, 2, 3 and 4. (B) Side view of Electrodes 1, 2, 3 and 4.

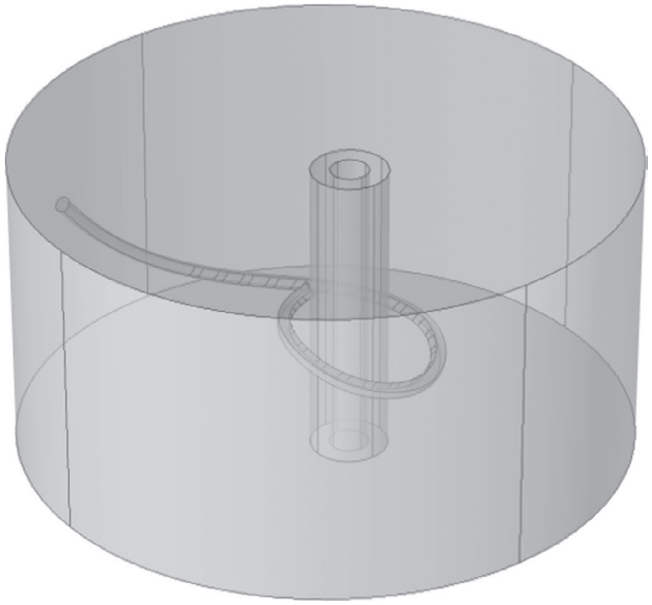

FIGURE 3 | Complete model setup for the CI-EIT validation study (Electrode 1, Test Location 1). A similar setup was used for the remaining electrodes and test locations.

Although CI electrode contact impedance measurements are a standard procedure available on all major CI platforms, the true contact impedance is influenced by several factors, including measurement approach (bipolar or monopolar stimulation), stimulation frequency and the person-specific electrode/electrolyte interface [22]. The contact impedance ranges from 10 kΩ at lower frequencies to less than 1 kΩ at higher frequencies [22, 23]. The minimum pulse repetition rate of Nucleus Freedom devices is 100 Hz [7], and the proposed CI-EIT system will operate below 1 kHz, resulting in a contact impedance range of approximately 2.5–4 kΩ [22]. The driving stimulus was chosen to be compatible with a Nucleus Freedom processor. It consisted of a biphasic pulse with an amplitude of 106.5 μA, phase duration of 400 μs, interphase gap of 7 μs and a stimulus period of 1200 μs. To validate the CI-EIT methodology, the electrode contact impedance was set to 4 kΩ for all electrodes.

EIDORS offers three image output resolutions, that is, 32×32, 64×64 and 128×128 pixels. The default resolution of 64×64 pixels was used to represent a 2D cross-section through the 3D model. This resulted in a pixel size of 0.25 mm. To investigate the localisation accuracy, the displacement of the inhomogeneity between iterations should at least be greater than the dimensions of a pixel. Further simulation constraints involved the inhomogeneity always to be encircled, but not intersected, by the electrode array. By displacing the inhomogeneity by 0.5 mm between iterations and adhering to the constraints, the test location coordinates (in mm) for each of the four electrode trajectories were selected, as summarised in Table 2.

The selected test location coordinates are shown, along with the respective electrode trajectories, in Figure 4. Only the CoG of the inhomogeneity at the different locations are indicated.

2.2 | CI-EIT Forward and Inverse Models

The forward solution and image reconstruction for the CI-EIT system were implemented in EIDORS v3.10 [18]. Two meshes were generated for each of the four electrode models and the associated inhomogeneity test locations as the same mesh may not be used for simulating data and reconstructing the image [24]. A custom element size was specified for both meshes to enable mesh refinement close to the electrodes. The mesh for the forward solution was selected to be finer than the mesh generated for the image reconstruction. The minimum and maximum element sizes in the models for the forward solution were 0.1 and 1.2 mm, respectively, with a maximum element growth rate of 1.35. This resulted in a mesh with an average of approximately 171,000 elements across the four electrodes and test locations. The minimum and maximum element sizes in the forward models for the inverse problem were 0.3 and 1.75 mm, respectively, with a maximum element growth rate of 1.45. This resulted in a mesh with an average of approximately 37,000 elements across the four electrodes and test locations.

The node coordinates and the corresponding element and boundary numbers of each mesh were exported from COMSOL

TABLE 1 | Model conductivity values.

Model domain	Cochlear structure	Conductivity (S/m)
Cylindrical volume	Cochlear fluid	1.5 [20]
Inhomogeneity (outer)	Modiolar bone	0.085 [21]
Inhomogeneity (inner)	Auditory nerve	0.333 [20]

TABLE 2 | Inhomogeneity location coordinates (in mm).

Test location	Electrode 1	Electrode 2	Electrode 3	Electrode 4
1	0,−1	−0.5,−1	−1.5,−1	−1,−1
2	0.5,−1	0,−0.5	−1,−1	−0.5,−1
3	1,−1	0.5,−0.5	−0.5,−1	0,−1
4	0,−0.5	0,0	0,−1	−2,−0.5
5	0.5,−0.5	0.5,0	0.5,−1	−0.5,−0.5
6	1,−0.5	1,0	−0.5,−0.5	0,−0.5
7	1.5,−0.5	0,0.5	0,−0.5	0.5,−0.5
8	1,0	0.5,0.5	0.5,−0.5	0,0
9	1.5,0	1,0.5	1,−0.5	0.5,0
10	—	−0.5,1	0,0	—
11	—	0,1	—	—
12	—	0.5,1	—	—

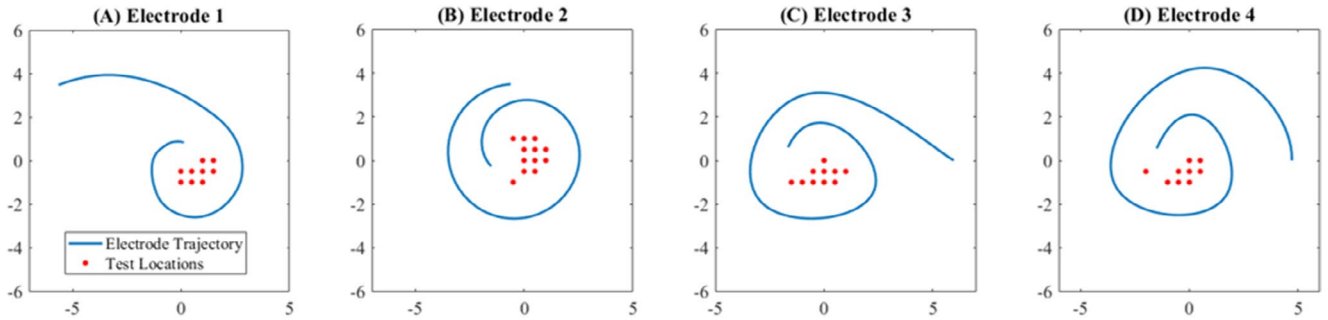

FIGURE 4 | The top view of the four electrode trajectories: (A) Electrode 1, (B) Electrode 2, (C) Electrode 3 and (D) Electrode 4, and corresponding test locations (in mm) from Table 2.

to EIDORS to generate a forward model according to the EIDORS object structure definitions [18].

2.3 | CI-EIT Measurement Strategy

Serialized EIT driving protocols usually consist of a single current source and voltage measurement unit, which is then multiplexed between the electrodes in a predefined pattern. Common serialized driving patterns include adjacent, cross, polar opposite and pseudo-polar patterns [25]. From these, the most common is the adjacent drive, although it has the poorest sensitivity to internal changes in resistivity. The subsequent patterns all aim to improve sensitivity [26]. The traditional adjacent protocol involves the stimulation between two adjacent electrodes while measurements are taken at the remaining electrode pairs. This corresponds to the bipolar stimulation protocol available in CI devices.

The proposed measurement strategy for the CI-EIT system is an adapted version of the traditional adjacent stimulation protocol. Traditionally, the number of adjacent measurements per cycle is given by $N-3$, where N is the number of electrodes. Accordingly, a total of $N(N-3)$ measurements can be taken with this stimulation protocol. Consider the diagrammatic visualisation of the CI electrode array in Figure 5, with electrodes $E = 1, 2, \ldots N$, numbered from the basal end (where $E = 1$) to the most apical electrode, where the proposed CI electrode model has $N = 22$. Traditionally, electrodes E_{22} and E_1 would have been the final stimulation or measurement pair in a specific measurement cycle. In the context of the CI electrode array, it was decided to discard this electrode pair, as the distance between them causes

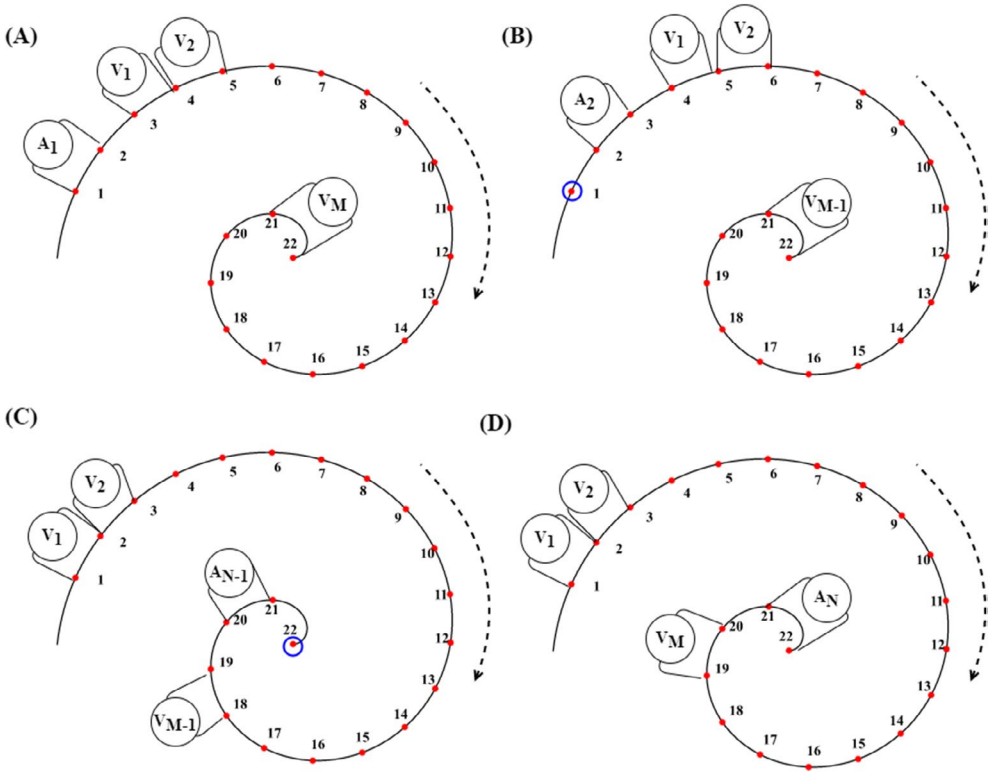

FIGURE 5 | The adjusted adjacent stimulation protocol for CI-EIT. (A) The first measurement cycle is similar to the traditional adjacent protocol with electrode pair E_1–E_2 as the stimulating electrodes, and the remainder of the electrode pairs employed for measurements, V_1–V_M. (B) The second measurement cycle in the adapted adjacent protocol. As the electrode pair E_{22}–E_1 is discarded, electrode E_1 is not used in this measurement cycle. A total of V_{M-1} measurements are taken. (C) The second to last measurement cycle is similar to the second measurement cycle as described in (B), with electrode E_{22} not used in the measurement cycle. Similarly, a total of V_{M-1} measurements are taken. (D) The final measurement cycle involves electrode pairs E_{N-1}–E_N and not E_N–E_1 as in the traditional protocol, essentially losing a measurement cycle.

large outliers in the simulated data and subsequent distortion of the reconstructed images. Accordingly, the adjacent stimulation protocol, as defined in EIDORS, could not be used as is, requiring the implementation of an adapted version. The adapted adjacent stimulation protocol operated like the traditional adjacent stimulation protocol, without the involvement of the measurement pair E_{22} and E_1 for any of the stimulation patterns. This stimulation protocol requires at least four electrodes.

The maximum total number of measurements for the CI-EIT system is given by:

$$M = (N-1)(N-4) + 2, \tag{1}$$

resulting in 380 measurements for a 22-electrode configuration, as opposed to 418 measurements when using the traditional adjacent drive.

In the design process of an EIT system, one of the objectives when choosing the stimulation current level is to maximize the sensitivity while adhering to patient safety restrictions. Higher EIT current levels result in higher sensitivity to internal changes in conductivity [3]. However, in CI systems, there is a restriction on the maximum current level that can be delivered to a user before discomfort is experienced, which is referred to as the comfortable loudness level (C level) [7]. Accordingly, the upper limit for the stimulation current of the CI-EIT system is the user's C level.

Stimulating at or just below threshold would be the hypothetical worst-case scenario for which the methodology could be validated, and therefore, a current amplitude that is typically below the auditory threshold of CI users was chosen. A threshold level of 100 μA is assumed for this study [27], but the specific threshold of a user can be obtained through a standard mapping procedure and incorporated into the image reconstruction procedure to enhance person-specific results.

2.4 | CI-EIT Simulated Measurements

The boundary data sets for the feasibility study are generated through the forward solution of the finer mesh, as discussed in Section 2. The simulated homogeneous (v_r) and inhomogeneous (v_i) data sets for all test locations in Table 2 were generated. The simulated data are noise-free, but actual CI-EIT measurements would be subjected to hardware-induced and physiological noise. Noise is added to the simulated measurements, v, such that

$$v_n = v\left(1 + \text{rand}\left(\zeta_P\right)\right) + \text{rand}\left(\zeta_a\right), \tag{2}$$

where v_n is the measurement set with noise, ζ_P is proportional noise and ζ_a is additive noise [28]. To simulate in vivo conditions, noise levels are set to $\zeta_P = 0.01\,\%$ and $\zeta_a = 2\mu V$ for low-noise and $\zeta_P = 0.02\,\%$ and $\zeta_a = 5\mu V$ for high-noise situations

[29]. The noise parameters are drawn randomly from a Gaussian distribution with zero mean and variance ζ.

2.5 | Image Reconstruction

The EIT problem is ill-conditioned and ill-posed. Regularisation techniques are commonly used to improve the ill-posed inverse problem by imposing additional constraints by introducing image priors. A prior carries assumptions or information about the conductivity distribution that constrain the set of feasible impedance distributions. This is achieved by allowing the reconstruction process to use pre-knowledge of the properties of the medium, such as the expected smoothness of the solution or known anatomical features, to improve the solution. The inclusion of priors leads to the introduction of another parameter, referred to as the hyperparameter (λ), which controls the trade-off between image conformance to the data or the prior [30]. For the CI-EIT feasibility study, a difference imaging approach was used for initial verification of the technique and for finding the most robust reconstruction parameters. Even though difference images of the cochlea could potentially be of clinical value over an extended period of time for evaluating changes within the cochlea, it would not necessarily be possible to obtain a homogeneous data set for once-off calculation of the modiolar CoG. Accordingly, a static or absolute reconstruction was also considered. For the image reconstruction process, a measured boundary data vector defined as $y = v - v_r$ for difference imaging, and $y = v$ for absolute imaging is required.

For the difference imaging, the one-step Gauss-Newton approach is followed [31]. The reconstructed image representing the conductivity distribution can be modelled by

$$\hat{x} = \left(J^T \mathrm{W} \mathrm{J} + \lambda^2 R\right)^{-1} \mathrm{J}^T \mathrm{W} y = \mathrm{B} y, \tag{3}$$

where $\hat{x}$ is the reconstructed conductivity distribution, J is the Jacobian matrix, R the regularization matrix, λ the scalar hyperparameter and W a model of the measurement accuracy [32]. The choice of prior and λ greatly influences the quality of the reconstructed image, but the optimal selections are not yet well established in the field of micro-electrode array EIT [10], and by extension for CI-EIT problems.

The absolute image reconstruction was implemented with an iterative Gauss-Newton solver using the parameters obtained from the difference imaging results.

2.6 | Image Reconstruction Parameter Analysis

A previous study demonstrated the applicability of NOSER and Tikhonov priors for micro-electrode array EIT [10], and therefore, these priors were selected for the present study. The Tikhonov prior introduces smoothness by assuming that the underlying conductivity distribution changes gradually rather than abruptly. For this reason, it tends to blur boundaries where there are sharp conductivity changes or localised features. The NOSER prior, on the other hand, favours solutions where the conductivity remains homogeneous by scaling a baseline conductivity. This emphasises localised contrasts better than the Tikonov prior. An objective measure to determine the most suitable combination of prior and λ is required. To this end, the sensitivity of modiolus CoG localisation error in response to prior and λ changes is assessed.

To obtain the CoG from the reconstructed image, the 3D reconstruction was sliced at the average height of the electrodes in the array to obtain a 2D 64×64 pixel image. As the ROI in the CI-EIT problem will always be within the electrode array, a mask encircling the electrodes for each array was applied to the image. The electrode trajectories and mask boundaries are illustrated in Figure 6. All pixel values outside of the boundary of the mask are set to zero.

After applying the mask, a thresholded binary image, $\hat{x}_t$, was created. As the inhomogeneity is less conductive than the background, the pixels of interest in the difference images will have a negative value. Accordingly, for the difference images, the 1/4-minimum amplitude set of the image was determined such that:

$$\hat{x}_{t,i} = \begin{cases} 1 & \text{if } \hat{x}_i \leq \frac{1}{4}\min(\hat{x}) \\ 0 & \text{otherwise} \end{cases} \tag{4}$$

where $\hat{x}_i$ is the i^{th} pixel of the reconstructed image. The thresholding of absolute images posed a challenge as the inhomogeneity will not necessarily have a negative value; however, image artefacts with negative values might be present in some cases. In either case, using a 1/4-minimum amplitude set is unfavourable, as the pixels falling within the range are very few or none at all. Accordingly, an alternative approach to thresholding absolute images was developed. The approach entailed finding the

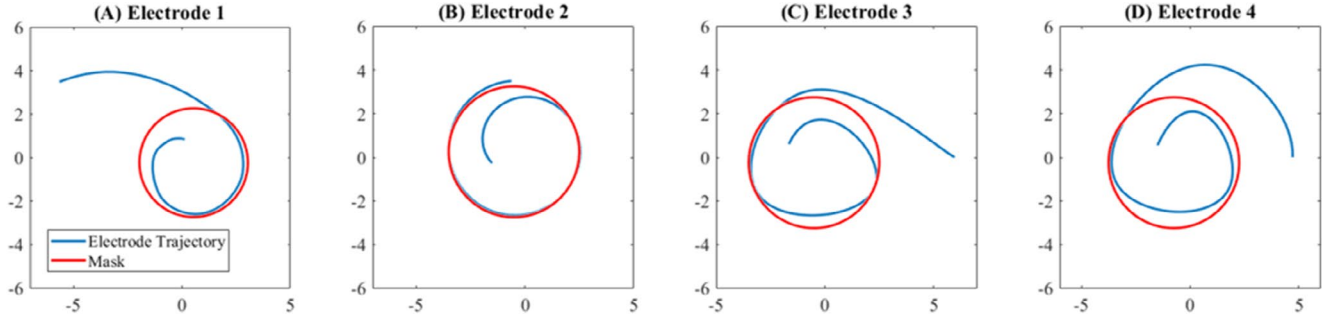

FIGURE 6 | The top view of the four electrode trajectories: (A) Electrode 1, (B) Electrode 2, (C) Electrode 3 and (D) Electrode 4, and corresponding masks.

midpoint of the pixel data set, from which an appropriate threshold variable could be heuristically determined. The thresholding of the absolute images is accordingly implemented such that:

$$\hat{x}_{t,i} = \begin{cases} 1 & \text{if } \hat{x}_i \le \alpha \times \frac{1}{2}\left(\max(\hat{x}) - \min(\hat{x})\right) \\ 0 & \text{otherwise} \end{cases} \quad (5)$$

where α is the threshold variable.

From the binary image, the area A was found as the largest cluster of connected pixels with a value of 1. The CoG of A was calculated as the centroid of the smallest rectangular bounding box encompassing the area. The localisation error was determined by

$$\xi = \frac{\sqrt{\left(r_{x,\text{rec}} - r_{x,\text{true}}\right)^2 + \left(r_{y,\text{rec}} - r_{y,\text{true}}\right)^2}}{\sqrt{d_x^2 + d_y^2}}, \quad (6)$$

where r_{true} is the true CoG coordinates as summarized in Table 2, r_{rec} is the CoG of A and d_x and d_y are the model dimensions.

Figure 7 illustrates the image analysis procedure. The regions of interest in all of the models under investigation are the model boundary, mask boundary, inhomogeneity boundary and CoG (Figure 7A). Figure 7B is a simplified representation of a reconstructed image with no artefacts, while Figure 7C shows the masked image. It can be observed that all of the pixels outside of the mask are set to zero. The masked image is then subjected to the threshold procedure, resulting in the binary image in Figure 7D. The largest cluster of connected pixels with a value of one is then determined from the binary image (in this simplified representation, there will only be one cluster of pixels). The smallest rectangle encompassing the cluster, or bounding box, is then found, as indicated in Figure 7E. The CoG of the pixel cluster is then found as the centroid of the bounding box.

The effect of λ on the localisation ability of the EIT system is investigated for the difference image reconstruction through a heuristic approach [30], after which the optimal λ is determined by the L-curve method [33]. The L-curve method is a graphical tool to determine the optimal regularisation parameter. It shows the trade-off between the norm of the regularised solution and the norm of the residuals (the difference between the observed and predicted data). It typically shows an L shape where the vertical part corresponds to the solution norm being large, that is, over-fitting to the noisy data, and the horizontal part corresponds to the residual norm being large, that is, over-smoothing and loss of data features. The inflexion point indicates where the regularisation parameter provides an optimal balance between the two.

The heuristic approach entails the solution of the inverse problem at 10 λ values ranging from 5×10^{-2} to 5×10^{-11}, decreasing in multiples of 10^{-1}, for all test locations and each of the four electrode trajectories. The simulation was repeated for the no- and low-noise data sets. The RMSE of the localisation errors was then calculated for each λ and prior. The λ with the lowest RMSE for each prior was identified as the most favourable value. The optimal λ obtained through the L-curve method is used to verify the heuristic results. The image reconstruction process was repeated for the no-, low- and high-noise measurements at the optimal λ.

From the results of the difference imaging analysis, the more robust prior and optimal λ is used in the absolute image reconstruction analysis. The optimal λ is heuristically verified for applicability to the absolute scenario by following the RMSE of the localisation error approach. The absolute image reconstruction at the verified optimal λ is conducted for the no-, low- and high-noise measurements.

2.7 | Statistical Analysis

Two important factors that must be accounted for in a CI-EIT system are noise and electrode trajectory variability. A statistical analysis was conducted to investigate the effect of these factors on the CoG localisation performance.

The sensitivity of the CoG localisation error to the presence of noise was assessed by comparing the localisation error among the no-, low- and high-noise data sets at the optimal λ. A paired t-test was conducted to assess whether a significant variability in localisation error can be observed between the no- and low-noise, and no and high noise data sets, respectively.

An ANOVA analysis was conducted on the localisation error results of the four unique electrode trajectories to verify whether the CI-EIT approach can be reliably applied to various electrode trajectories and noise scenarios.

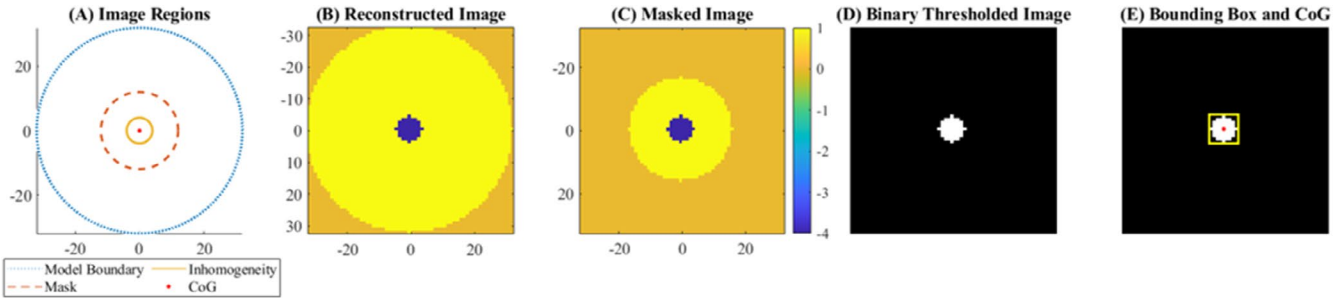

FIGURE 7 | The CI-EIT image analysis procedure which involves defining the required (A) image regions, (B) slicing the reconstructed image, (C) masking the image, (D) obtaining a binary thresholded image and (E) obtaining the bounding box and CoG.

The statistical analysis was conducted for the difference and absolute image reconstruction results. Finally, a paired *t*-test was conducted to verify whether the proposed methodology can be reliably applied to difference and absolute reconstruction scenarios.

3 | Results

3.1 | Difference Imaging

The difference image reconstruction parameter and statistical analysis results are presented and analysed as described in Section 2. The parameters for the absolute image reconstruction will be drawn from the conclusions of this analysis.

3.1.1 | Image Reconstruction Parameter Analysis

The localisation errors of the various test scenarios were determined by Equation (6). The RMSE of the localisation errors for the respective test locations at each λ value was calculated for the NOSER and Tikhonov priors under no-noise and low-noise conditions. The procedure was repeated for the four electrodes. The resultant RMSE of the localisation errors at each λ is shown in Figure 8. From the RMSE plots, it can be observed that the λ resulting in the lowest localisation errors for no- and low-noise is 5×10^{-4} and 5×10^{-7} when using the NOSER and Tikhonov priors respectively. The superior CoG localisation performance of NOSER relative to Tikhonov is demonstrated in the generally lower RMSE for all electrode trajectories.

The optimal λ was obtained for each test location for both priors and all electrodes using the L-curve method. The average λ for the two priors for all electrodes was calculated and is summarized in Table 3. The optimal λ values for each prior corresponded closely among the electrode models. The average for the NOSER prior is $\lambda_{\text{NOSER}} = 1.1212 \times 10^{-3}$ with a standard deviation of 2.1094×10^{-4}, and the average for the Tikhonov prior is $\lambda_{\text{Tikhonov}} = 5.0909 \times 10^{-7}$ with a standard deviation of 2.6898×10^{-8}. The optimal λ values are also in the range of the values observed in the heuristic experiment. $\lambda_{\text{Tikhonov}}$ corresponds closely to $\lambda = 5 \times 10^{-7}$ as observed in the heuristic experiment. λ_{NOSER} is in the same order of magnitude as the heuristically obtained value of $\lambda = 5 \times 10^{-4}$.

The averaged optimal λ values, as shown in Table 3, were used to reconstruct all of the test locations for the four electrodes at no-, low- and high-noise levels. The reconstructed images (before masking) for Test Location 1 at the averaged optimal λ are shown in Figure 9. The reconstructed CoG for each location was obtained after masking the image. The true CoG of the inhomogeneity is indicated by a "·" and the reconstructed CoG is indicated by an "x." Figure 9 shows the influence of ringing artefacts, which are areas representing a conductivity of opposite sign to the targeted reconstruction [34]. The inhomogeneity is of a conductivity smaller than the background conductivity, therefore resulting in a negative reconstructed change in conductivity ($\Delta\sigma$). The ringing artefacts would, therefore, be positive $\Delta\sigma$. According to the image scale, the inhomogeneity is expected to be dark blue, whereas the ringing artefacts are the bright yellow regions. Even though ringing artefacts are unfavourable, they did not have a negative influence on the determination of the 1/4-minimum amplitude set for the CoG localisation. Another artefact that can be observed in the reconstructed images is the presence of large regions of a similar conductivity to that of the reconstructed inhomogeneity. As opposed to the ringing artefacts, these artefacts distort the true shape of the inhomogeneity and may result in faulty detection of the CoG. However, using

TABLE 3 | The average λ for the NOSER and Tikhonov priors for all electrodes.

Electrode	NOSER	Tikhonov
1	9.5965×10^{-4}	5.4083×10^{-7}
2	1.4289×10^{-3}	4.9006×10^{-7}
3	1.0164×10^{-3}	4.8375×10^{-7}
4	1.0799×10^{-3}	5.2170×10^{-7}

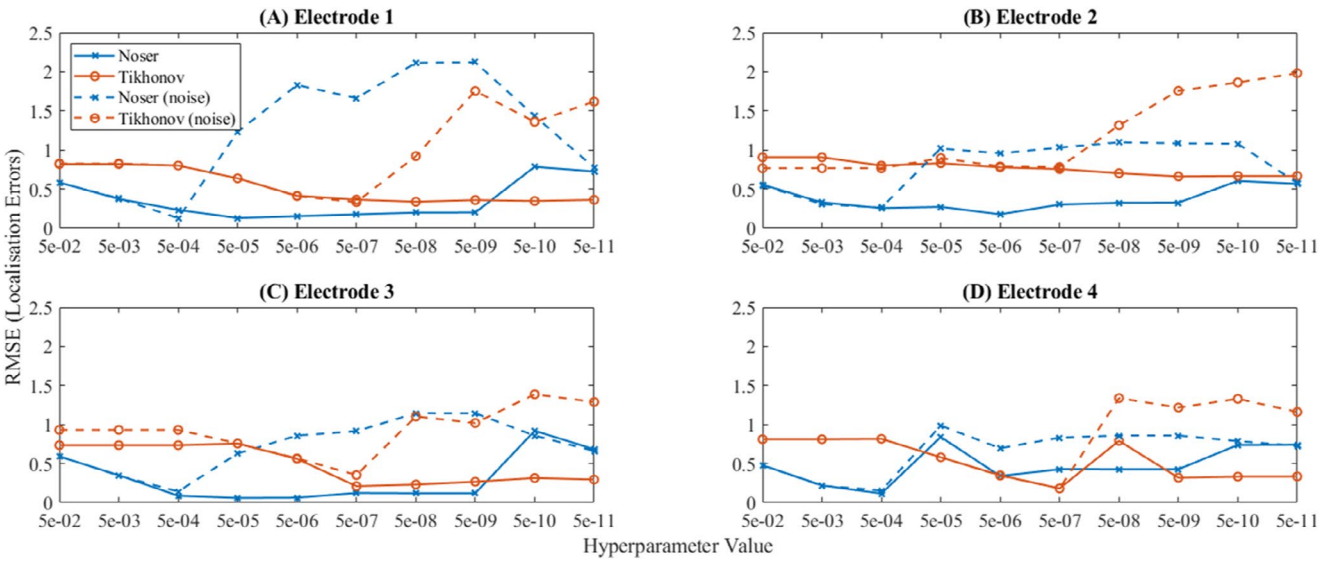

FIGURE 8 | RMSE of the localisation errors at the respective hyperparameters for the four electrode models.

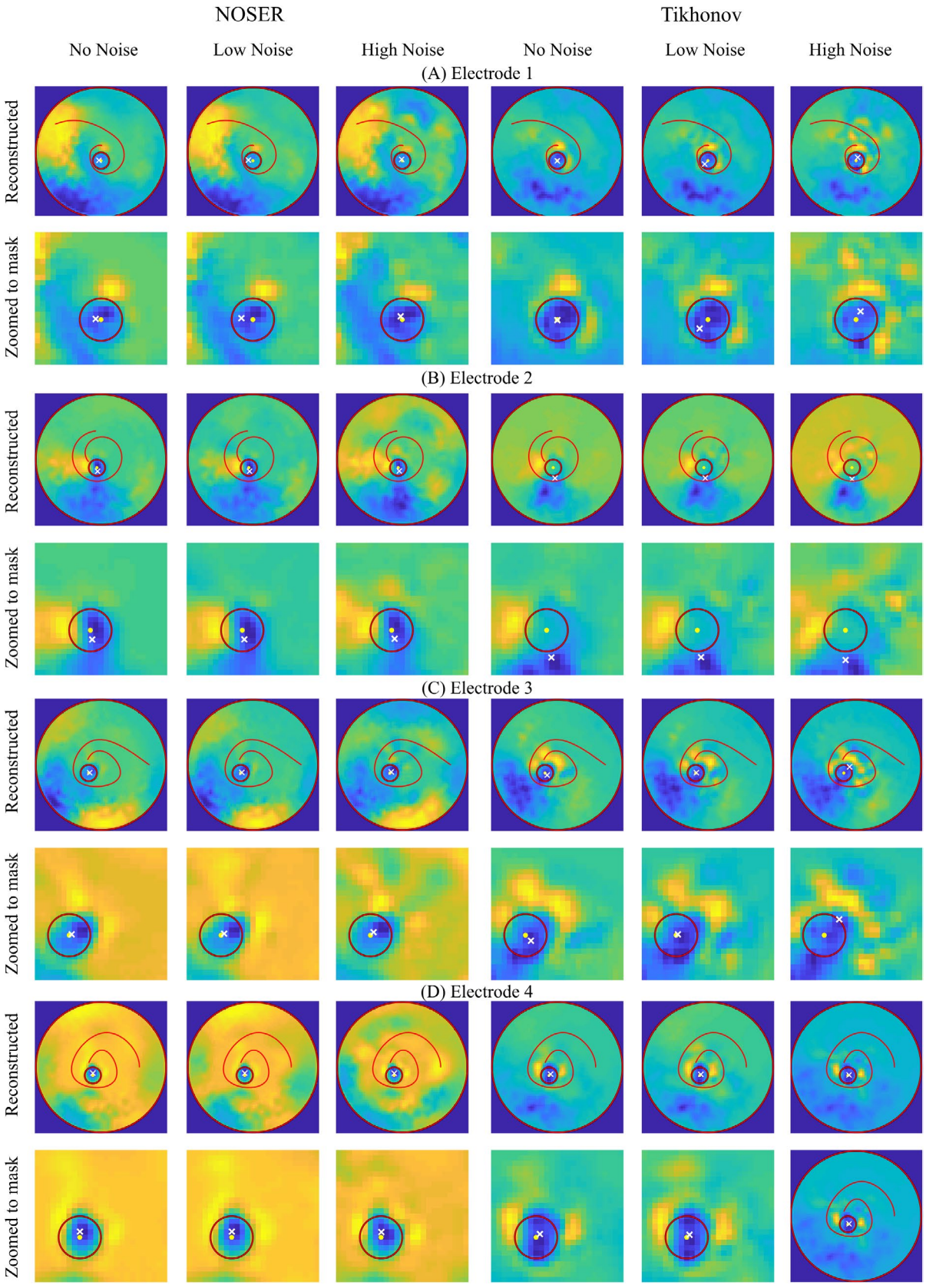

FIGURE 9 | Reconstructed and zoomed to masked ROI images for Test Location 1 at the averaged optimal λ, with (A) Electrode 1, (B) Electrode 2, (C) Electrode 3 and (D) Electrode 4 for NOSER and Tikhonov priors respectively in no-, low- and high-noise scenarios. All images show the original reconstructions before masking. The white "x" indicates the reconstructed CoG, and the yellow "·" indicates the true CoG. The red circles indicate the outlines of the model and the inhomogeneity, respectively. All images are scaled between the maximum $\Delta\sigma$ (bright yellow) and minimum $\Delta\sigma$ (dark blue).

prior knowledge about the modiolus position relative to the electrode array to mask the raw reconstructed image notably improves the CoG localisation ability of the CI-EIT system.

The average localisation error for each of the electrodes using the respective priors is shown in Figure 10. The figure suggests that the NOSER prior is more robust to noise than the Tikhonov prior, with smaller variations in localisation error for different noise levels. The localisation errors for all electrode trajectories using the NOSER prior are also less than those of the Tikhonov prior. The NOSER prior also appears to be more robust against large variations in vertical electrode displacement, especially considering the results from Electrode 2 in Figure 10. The localisation error using the Tikhonov reconstruction, in this case, is considerably higher than with the NOSER prior. This can also be observed in Figure 9B, where the reconstructed CoG (indicated by the "x") for the Tikhonov prior lies outside of the bounds of the inhomogeneity. This is not the case for any of the other reconstructed CoG locations.

Considering the electrode trajectories in Figure 2 and the localisation results in Figure 10B, a parallel can be observed between greater vertical electrode misalignment and higher localisation errors using the Tikhonov prior, especially in the high-noise scenarios. The association is not as apparent in the localisation errors using the NOSER prior.

3.1.2 | Statistical Analysis

From Figure 9, it can be observed that noise degrades the quality of the reconstructed image in terms of image artefacts and, to a lesser extent, inhomogeneity shape deformation. However, the influence on the localisation performance is not clear. Accordingly, a paired *t*-test was used to evaluate the noise sensitivity of the four electrode models using the two different priors. A paired *t*-test was conducted between the no-noise localisation errors and the low- and high-noise localisation errors, respectively. The results from the paired *t*-tests indicated no significant difference between localisation errors from reconstructed images subjected to low- or high-noise, respectively, as opposed to no-noise scenarios at a 1% significance level. Even though the two priors appeared to have comparable performance under low-noise scenarios, NOSER has superior performance in high-noise scenarios with $p_{\text{NOSER}} > p_{\text{Tik}}$ for all electrodes.

A one-way, unbalanced ANOVA was conducted on the localisation errors of the four electrode models in a no-noise scenario for the NOSER and Tikhonov priors, respectively. No significant difference was observed between localisation errors when using the NOSER prior ($p = 0.0768$). In contrast, the value of $p = 3.3413 \times 10^{-13}$ indicates a significant difference in reconstructed CoG localisation when using the Tikhonov prior. From the results of the ANOVA tests, it was evident that the choice of prior has a significant influence on the reliability of the localisation error among electrode trajectories.

3.2 | Absolute Imaging

From the difference imaging results in Section 3.1, it was found that a NOSER prior results in more reliable CoG localisation among electrode trajectories. Accordingly, it was decided to investigate the viability of CI-EIT absolute image reconstruction with the NOSER prior. The L-curve method resulted in an optimal $\lambda_{\text{NOSER}} = 1.1212 \times 10^{-3}$. For the absolute reconstruction, the optimal λ will be set to 0.001. This value was verified heuristically for the absolute case by finding the inverse solution at five values of λ ranging from 1×10^{-1} to 1×10^{-5}, decreasing in multiples of 10^{-1}, for all test locations and each of the four electrode trajectories at no- and low-noise. Once the optimal λ is verified, image reconstruction was conducted for the no-, low- and high-noise cases.

3.2.1 | Image Reconstruction Parameter Analysis

The localisation errors for the various test scenarios were determined by Equation (6). The RMSE of the localisation errors for the respective test locations at the five λ values was calculated for the NOSER prior under no-noise and low-noise conditions. The resultant RMSE of the localisation errors at each λ for the four electrode trajectories are shown in Figure 11. In Figure 11 the average localisation errors for the no- and low-noise scenarios among the four electrode trajectories are also indicated. From the average RMSE plot, it can be observed that the λ resulting in the lowest localisation errors for the no-noise case is 1×10^{-5}, but poor performance can be observed in the low-noise scenario with the highest average RMSE. The average RMSE for a λ of 1×10^{-2} and 1×10^{-3} corresponds closely, with values of 1.0788 and 1.0961 respectively. From this, the average RMSE for $\lambda = 1 \times 10^{-3}$ is 1.6%

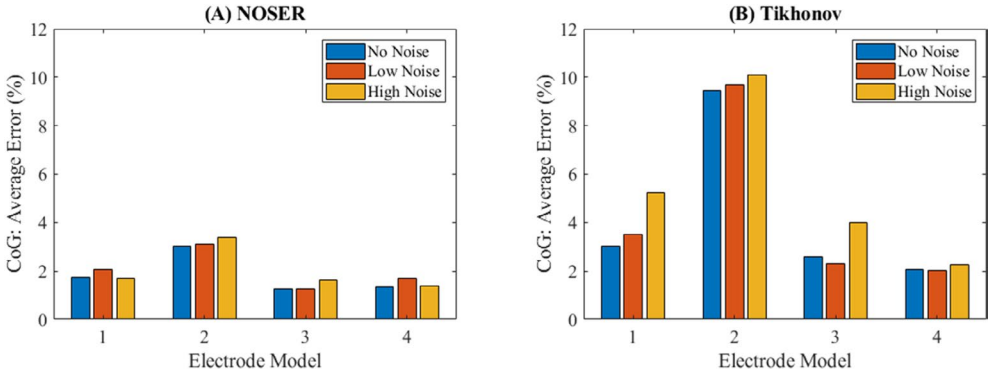

FIGURE 10 | The average localisation errors over the various test locations for each electrode model, using (A) NOSER and (B) Tikhonov priors and optimal hyperparameters.

higher than for a $\lambda = 1 \times 10^{-2}$. However, $\lambda = 1 \times 10^{-3}$ results in the lower average RMSE localisation errors in the no-noise scenario. The above-mentioned observations lead to the decision to continue with $\lambda = 1 \times 10^{-3}$ as the hyperparameter for the absolute image reconstruction, which corresponds to the optimal λ obtained from the difference imaging parameter analysis.

The optimal λ and the NOSER image prior were used to reconstruct absolute images for all of the test locations for the four electrode trajectories at no-, low- and high-noise levels. From the reconstructed images, the threshold variable for Equation (5) was heuristically determined and applied in the CoG localisation process throughout the test cases as $\alpha = 0.85$. The reconstructed images (before masking) for Test Location 1 of all four electrode trajectories are shown in Figure 12. Figure 12 also shows the reconstructions zoomed to the masked ROI. As with the difference imaging results in Figure 9, the effect of ringing artefacts can clearly be observed but does not have a detrimental influence on the CoG localisation. Masking of the image also reduced the effects of artefacts with similar conductivity to the inhomogeneity.

The average localisation error for each of the electrode trajectories subjected to different noise levels for absolute and difference imaging is shown in Figure 13. It can be observed that the absolute reconstruction have a higher average localisation error than the difference imaging results, especially for Electrode 2 where the variability in vertical electrode displacement is the most apparent. The higher error in absolute image reconstruction is to be expected as it is more susceptible to noise and modelling mismatches than difference imaging [35].

3.2.2 | Statistical Analysis

To evaluate the noise sensitivity of the absolute reconstruction with a NOSER prior at the optimal λ, a paired t-test was conducted between the no- and low-noise, and no and high noise localisation errors for each electrode. The results from the paired t-tests indicated no significant difference between localisation errors from reconstructed images subjected to no- and low-noise and no and high noise at a 1% significance level. A one-way unbalanced ANOVA was conducted for the no-noise scenario between the localisation errors for all four electrode trajectories to verify whether the absolute imaging technique could be reliably applied to different electrode trajectories. No significant difference was observed between the localisation errors with $p = 0.0119$.

Finally, a paired t-test was conducted between the localisation errors of the absolute and difference imaging for each electrode and noise level. No significant difference was observed at a 1% significance level.

4 | Discussion

The proposed CI-EIT system was modelled, analysed and validated in simulation. The simulation study was designed to investigate the viability of translating the proposed CI-EIT system to clinical application for augmenting present cochlear imaging techniques. The four unique electrode trajectories and associated inhomogeneities, as well as the adapted adjacent stimulation protocol, were successfully implemented in EIDORS. Typical cochlear tissue conductivity values, clinically feasible stimulation parameters and varying levels of noise were used in a simplified geometry to emulate the in vivo environment.

To implement a robust CI-EIT system, the sensitivity of the reconstructed CoG localisation to different image reconstruction priors and hyperparameters was investigated. For both the NOSER and Tikhonov priors, the desired λ obtained through the heuristic approach corresponded closely to the optimal λ obtained by using the L-curve method. The λ for different electrode configurations also corresponded closely, allowing for a generalised average value to be used in further simulations.

The CI-EIT reconstructed images using the optimal λ in no-, low- and high-noise scenarios for both priors yielded distinguishable images of the simulated modiolus (cylindrical inhomogeneity). Image artefacts are pertinent in the reconstructed images, but the knowledge of the ROI allows for image masking to ensure improved localisation of the modiolus.

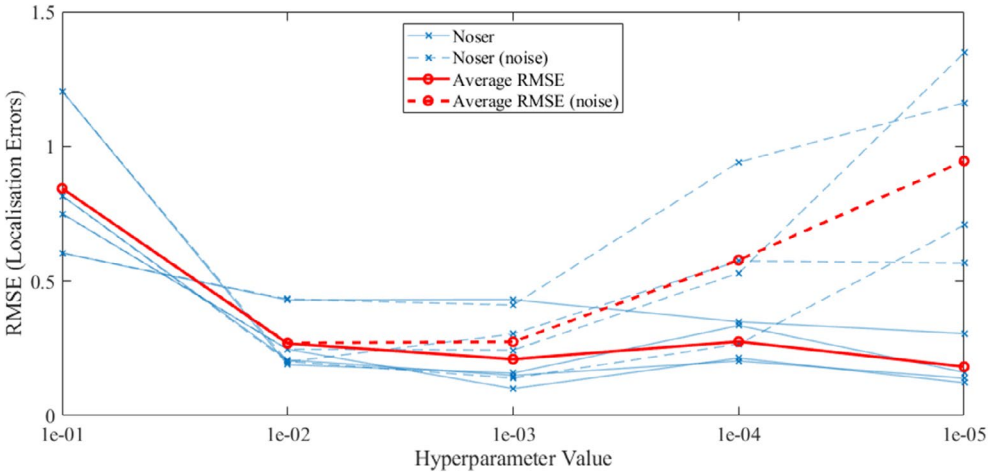

FIGURE 11 | RMSE of the localisation errors for the absolute reconstructions at the respective hyperparameters for the four electrode models. The average RMSE localisation errors for the no- and low-noise scenarios are indicated in the overlaying bold lines.

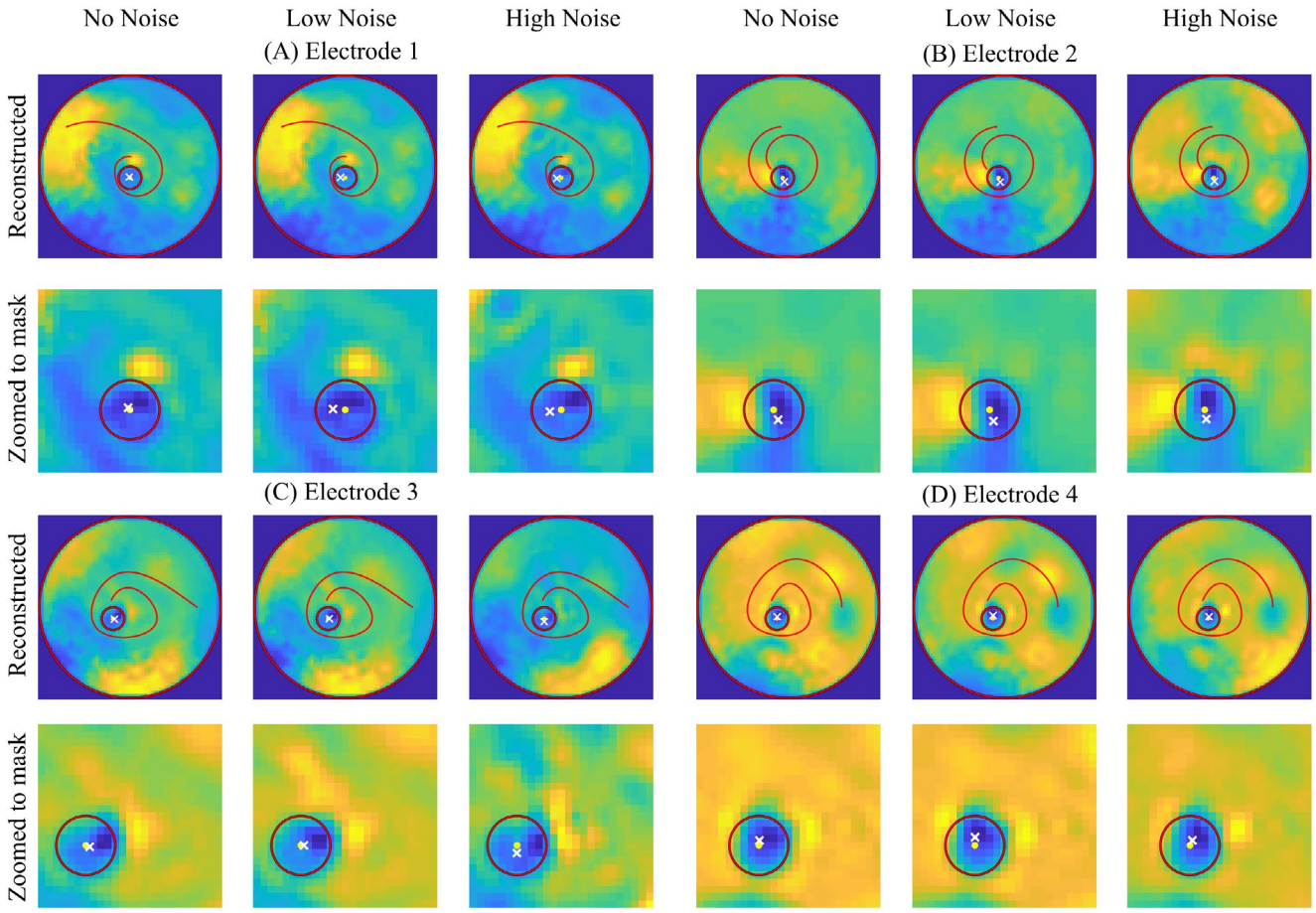

FIGURE 12 | Reconstructed images (before masking) for Test Location 1 at the averaged optimal λ, with (A) Electrode 1, (B) Electrode 2, (C) Electrode 3 and (D) Electrode 4 for the NOSER prior respectively in no-, low- and high-noise scenarios. The white "x" indicates the reconstructed CoG, and the yellow "·" indicates the true CoG. The red circles indicate the outlines of the model and the inhomogeneity, respectively. All images are scaled between the maximum $\Delta\sigma$ (bright yellow) and minimum $\Delta\sigma$ (dark blue).

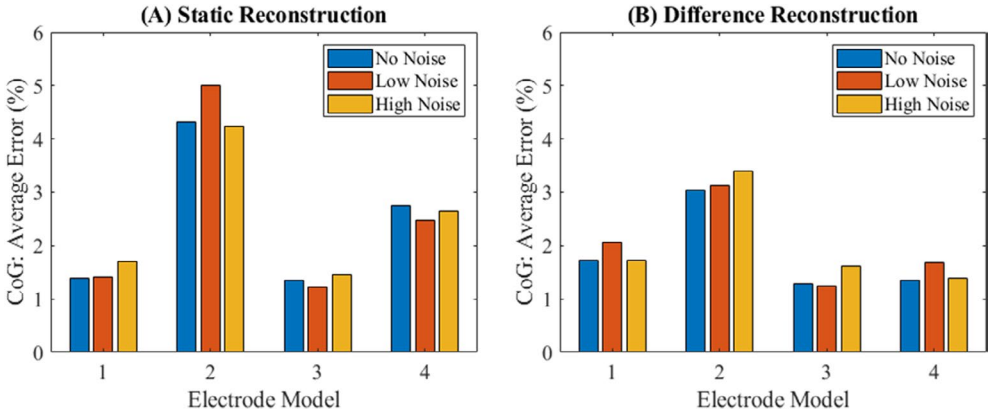

FIGURE 13 | The average localisation errors over the various test locations for each electrode model, using a NOSER prior and optimal hyperparameters for (A) absolute and (B) difference imaging.

Using the difference imaging technique for each electrode model, no significant difference was observed between the CoG localisation with and without the presence of noise. Accordingly, for a specific electrode configuration, both priors performed well at the optimal λ, although the NOSER prior seemed to exhibit superior localisation performance. When analysing the localisation performance among electrode trajectories, no significant differences were observed among NOSER reconstructions. However, a significant difference was observed among reconstructions when using the Tikhonov prior. The results demonstrate that NOSER exhibits more robust performance relative to the Tikhonov priors in CI-EIT image reconstruction for various noise scenarios and electrode trajectories. This outcome is consistent with the characteristics of the NOSER prior. First,

it emphasises contrast over smoothness, which is appropriate for the present CI-EIT study, where the modiolus is a localised structure with a different conductivity from the rest of the domain. Second, the NOSER prior tends to perform well with circular structures, such as the simulated modiolus in this study, because of the radially symmetric mathematical principles that it uses [36].

The parameters for the absolute imaging were selected from the results of the difference imaging analysis. Due to the more robust nature of the NOSER prior in the modelled CI-EIT setting, this prior along with the optimal λ was used throughout. No significant difference was observed between the CoG localization with and without the presence of noise. There was also no significant difference between the CoG localisation performance among electrode trajectories or between difference and absolute imaging, indicating that the CI-EIT could be robustly applied for different CI electrode array trajectories and reconstruction scenarios.

5 | Conclusion

This study demonstrated the viability of CI-EIT as a method to obtain more information about the inner structure of the cochlea despite the multiplaner electrode distribution, conductive media layer in which the electrodes are located and pulsatile driving stimuli. The proposed CI-EIT methodology favours the use of the NOSER prior above the Tikhonov prior with a hyperparameter $\lambda = 0.001$ to best estimate the CoG of the modiolus. This setup results in localisation errors of 5.5% for the absolute imaging method and 4% for the difference imaging method. The significance level for the difference between the two is less than 1% suggesting that either may be used to determine the CoG of the modiolus. Thus, the clinical implementation of this system may provide valuable in vivo insights into the unique, person-specific interior structures of the cochlea, with essentially no cost to the user.

Author Contributions

Friedemarie Fourie and Tania Hanekom conceived the study. Friedemarie Fourie performed the experiments and analysed the data. Friedemarie Fourie and Joshua Thiselton designed and validated the models and wrote the first version of the manuscript, with Tania Hanekom providing critical revisions. Tania Hanekom supervised the project and coordinated research activities. All authors contributed to the refinement and revision of the final manuscript.

Ethics Statement

This research was conducted with clearance from the Research Ethics Committee of the Faculty of Health Sciences, University of Pretoria.

Conflicts of Interest

The authors declare no conflicts of interest.

Data Availability Statement

Data sharing is not applicable to this article as no new data were created or analyzed in this study.

References

1. G. Widmann, D. Dejaco, A. Luger, and J. Schmutzhard, "Pre-and Post-Operative Imaging of Cochlear Implants: A Pictorial Review," *Insights Into Imaging* 11, no. 1 (2020): 93.

2. T. Malherbe, T. Hanekom, and J. Hanekom, "Constructing a Three-Dimensional Electrical Model of a Living Cochlear Implant User's Cochlea," *International Journal for Numerical Methods in Biomedical Engineering* 32, no. 7 (2016): e02751.

3. B. H. Brown, "Electrical Impedance Tomography (EIT): A Review," *Journal of Medical Engineering & Technology* 27, no. 3 (2003): 97–108.

4. S. Mansouri, Y. Alharbi, F. Haddad, S. Chabcoub, A. Alshrouf, and A. Abd-Elghany, "Electrical Impedance Tomography—Recent Applications and Developments," *Journal of Electrical Bioimpedance* 12 (2021): 50–62.

5. S. Gabriel, R. W. Lau, and C. Gabriel, "The Dielectric Properties of Biological Tissues: III. Parametric Models for the Dielectric Spectrum of Tissues," *Physics in Medicine and Biology* 41 (1996): 2271–2293, https://doi.org/10.1088/0031-9155/41/11/003.

6. Q. Liu, T. Oh, H. Wi, E. Lee, J. Seo, and E. Woo, "Design of a Microscopic Electrical Impedance Tomography System Using Two Current Injections," *Physiological Measurement* 32 (2011): 1505–1516.

7. F. G. Zeng, S. Rebscher, W. Harrison, X. Sun, and H. Feng, "Cochlear Implants: System Design, Integration, and Evaluation," *IEEE Reviews in Biomedical Engineering* 1 (2008): 115–142.

8. C. McKay, K. Chandan, and I. Akhoun, "Can ECAP Measures Be Used for Totally Objective Programming of Cochlear Implants?," *Journal of the Association for Research in Otolaryngology* 14 (2013): 879–890.

9. J. Jossinet, E. Marry, and A. Montalibet, "Electrical Impedance Endo-Tomography: Imaging Tissue From Inside," *IEEE Transactions on Medical Imaging* 21, no. 6 (2002): 560–565.

10. D. Zhu, A. McEwan, and C. Eiber, "Microelectrode Array Electrical Impedance Tomography for Fast Functional Imaging in the Thalamus," *NeuroImage* 198 (2019): 44–52.

11. M. Faulkner, S. Hannan, K. Aristovich, J. Avery, and D. Holder, "Feasibility of Imaging Evoked Activity Throughout the Rat Brain Using Electrical Impedance Tomography," *NeuroImage* 178 (2018): 1–10.

12. S. Hannan, M. Faulkner, K. Aristovich, J. Avery, M. Walker, and D. Holder, "Imaging Fast Electrical Activity in the Brain During Ictal Epileptiform Discharges With Electrical Impedance Tomography," *NeuroImage: Clinical* 20 (2018): 674–684.

13. S. Hannan, M. Faulkner, K. Aristovich, J. Avery, M. C. Walker, and D. S. Holder, "In Vivo Imaging of Deep Neural Activity From the Cortical Surface During Hippocampal Epileptiform Events in the Rat Brain Using Electrical Impedance Tomography," *NeuroImage* 209 (2020): 116525.

14. S. Hannan, K. Aristovich, M. Faulkner, J. Avery, M. C. Walker, and D. S. Holder, "Imaging Slow Brain Activity During Neocortical and Hippocampal Epileptiform Events With Electrical Impedance Tomography," *Physiological Measurement* 42, no. 1 (2021): 014001.

15. Y. D. Jiang and M. Soleimani, "Capacitively Coupled Electrical Impedance Tomography for Brain Imaging," *IEEE Transactions on Medical Imaging* 38 (2019): 2104–2113.

16. W. Wimmer, C. Vandersteen, N. Guevara, M. Caversaccio, and H. Delingette, "Robust Cochlear Modiolar Axis Detection in CT," *Medical Image Computing and Computer-Assisted Intervention: MICCAI 2019*, Lecture Notes in Computer Science, vol. 11768, eds. D. Shen, T. Liu, T. M. Peters, et al. (Cham, Switzerland: Springer, 2019), 3–10.

17. J. K. Choong, A. J. Hampson, K. M. Brody, et al., "Nanomechanical Mapping Reveals Localized Stiffening of the Basilar Membrane After Cochlear Implantation," *Hearing Research* 385 (2020): 107846.

18. A. Adler and W. R. Lionheart, "Uses and Abuses of EIDORS: An Extensible Software Base for EIT," *Physiological Measurement* 27, no. 5 (2006): S25–S42.

19. E. Erixon, H. Högstorp, K. Wadin, and H. Rask-Andersen, "Variational Anatomy of the Human Cochlea: Implications for Cochlear Implantation," *Otology & Neurotology* 30, no. 1 (2009): 14–22.

20. C. C. Finley, B. S. Wilson, and M. W. White, "Models of Neural Responsiveness to Electrical Stimulation," in *Cochlear Implants: Models of the Electrically Stimulated Ear* (New York, NY: Springer, 1990), 55–96.

21. M. F. Suesserman, "Noninvasive Microelectrode Measurement Technique for Performing Quantitative, In Vivo Measurements of Inner Ear Tissue Impedances." PhD thesis, University of Washington, Washington; 1992.

22. C. Jiang, S. De Rijk, G. Malliaras, and M. Bance, "Electrochemical Impedance Spectroscopy of Human Cochleas for Modeling Cochlear Implant Electrical Stimulus Spread," *APL Materials* 8, no. 9 (2020): 091102.

23. X. Cheng, B. Wang, Y. Liu, Y. Yuan, Y. Shu, and B. Chen, "Comparable Electrode Impedance and Speech Perception at 12 Months After Cochlear Implantation Using Round Window Versus Cochleostomy: An Analysis of 40 Patients," *ORL; Journal for Oto-Rhino-Laryngology and Its Related Specialties* 80, no. 5–6 (2018): 248–258.

24. W. R. Lionheart, "EIT Reconstruction Algorithms: Pitfalls, Challenges and Recent Developments," *Physiological Measurement* 25, no. 1 (2004): 125–142.

25. A. Adler and A. Boyle, "Electrical Impedance Tomography: Tissue Properties to Image Measures," *IEEE Transactions on Biomedical Engineering* 64, no. 11 (2017): 2494–2504.

26. X. Shi, X. Dong, W. Shuai, F. You, F. Fu, and R. Liu, "Pseudo-Polar Drive Patterns for Brain Electrical Impedance Tomography," *Physiological Measurement* 27, no. 11 (2006): 1071–1080.

27. T. Strydom and J. J. Hanekom, "An Analysis of the Effects of Electrical Field Interaction With an Acoustic Model of Cochlear Implants," *Journal of the Acoustical Society of America* 129, no. 4 (2011): 2213–2226.

28. M. Jehl, K. Aristovich, M. Faulkner, and D. Holder, "Are Patient Specific Meshes Required for EIT Head Imaging?," *Physiological Measurement* 37, no. 6 (2016): 879–892.

29. N. Goren, J. Avery, and D. Holder, *Feasibility Study for Monitoring Stroke and TBI Patients* (London: University College London, 2015), 71.

30. B. Graham and A. Adler, "Objective Selection of Hyperparameter for EIT," *Physiological Measurement* 27, no. 5 (2006): S65–S79.

31. A. Adler and R. Guardo, "Electrical Impedance Tomography: Regularized Imaging and Contrast Detection," *IEEE Transactions on Medical Imaging* 15, no. 2 (1996): 170–179.

32. A. Adler, T. Dai, and W. R. Lionheart, "Temporal Image Reconstruction in Electrical Impedance Tomography," *Physiological Measurement* 28, no. 7 (2007): S1–S11.

33. P. C. Hansen, "Regularization Tools Version 4.0 for Matlab 7.3," *Numerical Algorithms* 46, no. 2 (2007): 189–194.

34. A. Adler, J. H. Arnold, R. Bayford, et al., "GREIT: A Unified Approach to 2D Linear EIT Reconstruction of Lung Images," *Physiological Measurement* 30, no. 6 (2009): S35–S55.

35. d T. Castro Martins, A. K. Sato, d F S. Moura, et al., "A Review of Electrical Impedance Tomography in Lung Applications: Theory and Algorithms for Absolute Images," *Annual Reviews in Control* 48 (2019): 442–471.

36. M. Cheney, D. Isaacson, J. Newell, S. Simske, and J. Goble, "NOSER: An Algorithm for Solving the Inverse Conductivity Problem," *International Journal of Imaging Systems and Technology* 2 (1990): 66–75.